On the kinematic deconvolution of the local neighbourhood luminosity function

C. Pichon, A. Siebert, O. Bienaymé

Mon. Not. R. Astron. Soc. **329,** 181–194 (2002)

On the kinematic deconvolution of the local neighbourhood luminosity function

C. Pichon,[1,2]★ A. Siebert[1] and O. Bienaymé[1]
[1]*Observatoire de Strasbourg, 11 rue de l'Université, 67000 Strasbourg, France*
[2]*Institut d'Astrophysique de Paris, 98 bis boulevard d'Arago, 75014 Paris, France*

Accepted 2001 August 31. Received 2001 July 5; in original form 1999 December 29

ABSTRACT

A method for inverting the statistical star counts equation, including proper motions, is presented; in order to break the degeneracy in that equation, it uses the supplementary constraints required by dynamical consistency. The inversion gives access to both the kinematics and the luminosity function of each population in three régimes: the singular ellipsoid, the constant ratio Schwarzschild ellipsoid plane-parallel models and the epicyclic model. This more realistic model is tailored to account for the local neighbourhood density and velocity distribution.

The first model is fully investigated, both analytically and by means of a non-parametric inversion technique, while the second model is shown to be formally its equivalent. The effect of noise and incompleteness in apparent magnitude is investigated. The third model is investigated by a 5D + 2D non-parametric inversion technique where positivity of the underlying luminosity function is explicitly accounted for.

It is argued that its future application to data such as the Tycho catalogue (and in the upcoming satellite *GAIA*) could lead – provided that the vertical potential and or the asymmetric drift or $w_\odot$ are known – to a non-parametric determination of the local neighbourhood luminosity function without any reference to stellar evolution tracks. It should also yield the proportion of stars for each kinematic component and a kinematic diagnostic to split the thin disc from the thick disc or the halo.

Key words: methods: data analysis – Hertzsprung–Russell (HR) diagram – stars: luminosity function, mass function – Galaxy: kinematics and dynamics – Galaxy: stellar content – Galaxy: structure.

1 INTRODUCTION

Most of our knowledge of the global structure of the Galaxy relies on the comparison of magnitude and colour star counts in different Galactic directions. Star counts alone do not allow us to solve the dilemma that a star of a given apparent magnitude can be either intrinsically faint and close by, or bright and distant. This problem may be addressed statistically by using the century-old equation of stellar statistics (von Seeliger 1898):

$$A_\lambda(m, \ell, b) = \int_0^\infty \Phi_\lambda(M)\rho(r, \ell, b)r^2\,\mathrm{d}r, \qquad (1)$$

where $A_\lambda(m, \ell, b)\,\mathrm{d}m\,\mathrm{d}\ell\,\mathrm{d}(\sin b)$ is the number of stars that have an apparent magnitude in the range $[m, m + \mathrm{d}m]$, $\Phi_\lambda(M)$ is the luminosity function (LF), which depends on the intrinsic magnitude, M, and the colour band λ, while $\rho(r, \ell, b)$ is the density at radius r (within $\mathrm{d}r$) along the line of sight in the direction given by the Galactic longitudes and latitudes (ℓ, b) [within the solid angle $\mathrm{d}\ell\cos(b)\,\mathrm{d}b$].

This equation cannot be solved or inverted (i.e., by determining both the stellar LF and the density law) except for a few simplified cases. For instance, with a 'homogeneous' stellar sample for which the absolute magnitudes of stars or, more precisely, their LFs are known, the density law along the line of sight can be recovered. A classical numerical technique (Mihalas & Binney 1981) has been proposed – the Bok (1937) diagram – while more rigorous treatments are required for small samples to stabilize the inversion so as to produce smooth solutions (Binney & Merrifield 1998). The converse situation is the determination of the LF assuming a known density law (see, for instance, recent studies of the faint end of the disc or halo main sequence based on deep star counts (Reid et al. 1996; Gould, Flynn & Bahcall 1998).

★E-mail: pichon@astro.u-strasbg.fr

A simple approach, developed largely in the 1980s, was to integrate equation (1) assuming some prior information concerning the stellar populations (see, e.g., Pritchet 1983, Bahcall, Soneira & Schmidt 1983, Buser & Kaeser 1985 and Robin & Crézé 1986). A frequent assumption is, for instance, to assume that the halo stars have the same LF as some low-metallicity globular clusters. Another approach consists in building a stellar LF from stellar evolution tracks and isochrones of various ages. This has been used to put constraints on the Galactic disc star formation rate (Haywood, Robin & Crézé 1997a,b).

Stronger a priori constraints may also be derived by requiring dynamical consistency, since the vertical kinematics of stars is related to the flattening of stellar discs or spheroidal components.

Since star counts alone, $A_\lambda(m, \ell, b)$, are not sufficient to constrain uniquely the Galactic stellar population models, it is expected that two (or more) distinct models will reproduce the same apparent star counts. However, this is not a real worry, since it is likely that adding some relevant extra a priori information must help to lift partially the degeneracy of the models.

In this paper it is shown that the degeneracy is lifted altogether when we consider, in addition to the star counts in apparent magnitude, the proper motions, μ_ℓ and μ_b. For a relatively general dynamically consistent model (stationary, axisymmetric and fixed kinematic radial gradients), the statistical equation counts may be formally inverted, giving access to *both* the vertical density law of each stellar population *and* their LFs. This is developed in Section 2, where we show how the vertical motions are related to the thickness of stellar components. The remaining degeneracy occurs only for a quadratic vertical potential. Otherwise – when the vertical component of the potential is known – the departures from quadratic behaviour define a characteristic scale that allows us to transform statistically the magnitudes into distances and proper motions into velocities. Similarly, the asymmetric drift and/or the vertical velocity component of the Sun provide a natural scale in energy, leading to the same inversion procedure.

For ideal star counts (infinitely deep and for an infinite number of stars), the inversion gives exactly the proportion of stars in each kinematic component, providing a direct diagnostic to split the thin disc from the thick disc or the halo, and its luminosity function $\Phi_\lambda(M)$ is recovered for each kinematic stellar component. This is a direct consequence of the supplementary constraints introduced by the requirement for dynamical consistency.

Section 2 presents the generalized stellar statistic equation which accounts for proper motions, and demonstrates the uniqueness of the inversion for two families of plane-parallel distribution functions: the singular velocity ellipsoid (Section 2.1) and a constant ratio velocity ellipsoid (Section 2.2), while Section 2.3 presents a basic description of the epicyclic model. Section 3 illustrates the inversion procedure on a fictitious superposition of four kinematically decoupled populations with distinct main-sequence turn-off magnitudes for the constant ratio velocity ellipsoid and the epicyclic models. Section 4 discusses the effects of truncation in apparent magnitude (i.e., completeness of the catalogue) in the recovered LF, as well as noise in the measurements. Finally, Section 5 discusses the applicability of the method to the Tycho-2 catalogue and to external clusters, and concludes the paper.

2 DERIVATION

The number of stars, dN, that have an apparent luminosity in the range $[L, L + \mathrm{d}L]$ in the solid angle defined by the Galactic longitudes and latitudes (ℓ, b) [within $\mathrm{d}\ell\,\mathrm{d}(\sin b)$], with proper motions μ_ℓ and μ_b (within $\mathrm{d}\mu_b$ and $\mathrm{d}\mu_\ell$) is given by

$$\begin{aligned}\mathrm{d}N \equiv\ & A_\lambda(L, \mu_l, \mu_b; l, b)\,\mathrm{d}\mu_\ell\,\mathrm{d}\mu_b\,\mathrm{d}\ell\cos b\,\mathrm{d}b\,\mathrm{d}L \\ =\ & \left\{\iiint \Phi^{\star}_\lambda[L_0, \beta]\left[\int f_\beta(\boldsymbol{r}, \boldsymbol{u})\,\mathrm{d}u_r\right] r^4\,\mathrm{d}r\,\mathrm{d}\beta\right\} \\ & \times \mathrm{d}\mu_\ell\,\mathrm{d}\mu_b\,\mathrm{d}\ell\cos b\,\mathrm{d}b\,\mathrm{d}L, \end{aligned} \tag{2}$$

where we have introduced the LF per unit bandwidth, $\Phi^{\star}_\lambda[L_0, \beta]$, which is here taken to be a function of the absolute luminosity, L_0, and of a continuous kinematic index, β. The variables $\boldsymbol{r}$, $\boldsymbol{u}$ are the vector position and velocity coordinates (u_r, u_ℓ, u_b) in phase-space relative to the local standard of rest, while $\boldsymbol{R}$ and $\boldsymbol{V}$ are those relative to the Galactic Centre. The relationship between $A_\lambda(L, \mu_l, \mu_b; l, b)$ and $\Phi^{\star}_\lambda[L_0, \beta]$ involves a double summation over β, and distance, r, along the line of sight. Here $f_\beta(\boldsymbol{r}, \boldsymbol{u})$ represents the β component of the distribution function of the assumed stationary axisymmetric equilibrium, i.e.,

$$f(\boldsymbol{r}, \boldsymbol{u}) = \int_0^\infty f_\beta(\boldsymbol{r}, \boldsymbol{u})\,\mathrm{d}\beta, \tag{3}$$

where f is decomposed over the basis of isothermal solutions f_β of the Boltzmann equation for the assumed known potential ψ. Equation (3) corresponds to a decomposition over isothermal populations of different kinematic temperatures, $\sigma^2 = 1/\beta$. Apart from this restriction, the shape of the distribution $f(E_z)$ could be anything. Note that equation (2) is a direct generalization of equation (1), since

$$\rho_\beta(r, \ell, b, \mu_\ell, \mu_b) \equiv r^2 \int f_\beta(\boldsymbol{r}, \boldsymbol{u})\,\mathrm{d}u_r$$

is by definition the density of stars (belonging to population β) which are at position $\boldsymbol{r} \equiv (r, \ell, b)$ within $\mathrm{d}r\,\mathrm{d}\ell\,\mathrm{d}(\sin b)$, with proper motion μ_b (within $\mathrm{d}\mu_b$) and μ_ℓ(within $\mathrm{d}\mu_\ell$). The extra summation on β which arises in equation (2) accounts for the fact that stars in the local neighbourhood come from a superposition of different kinematic populations which, as is shown later, can be disentangled. Note that $\Phi^{\star}_\lambda$ is defined here per unit absolute luminosity, L_0, and therefore

$$\Phi_\lambda[M(L_0)] = \frac{2\log(10)}{5} L_0 \int \Phi^{\star}_\lambda[L_0, \beta]\,\mathrm{d}\beta, \quad \text{where}$$

$$M(L_0) = -\frac{5}{2}\frac{1}{\log 10}\log\left(\frac{L_0}{\mathrm{L}_\odot}\right) + \mathrm{M}_\odot.$$

Since there is no convolution on λ (which is mute), it will be omitted from now on in the derivation. In Section 3, $B - V$ colours are reintroduced to demonstrate the inversion for a fictitious HR diagram. We shall also drop the $\star$ superscript, but will keep in mind that the LF is expressed as a function of the absolute luminosity, L_0.

This paper is concerned with the inversion of equation (2). We proceed in three steps. First, a simplistic Ansatz for the distribution function is assumed (corresponding to a stratification in height of uniform discs with a pin-like singular velocity ellipsoid), leading to a proof that, in this context, equation (2) has a well-defined unique solution which can be made formally explicit. A more realistic model is then presented, accounting for the measured anisotropy of the velocity ellipsoid. It is shown that, in the direction of the Galactic Centre, and if the velocity dispersions ratios are constant for all populations, this model is formally invertible following the

same route. Away from the Galactic Centre direction, the velocity components of the Sun are also accounted for to recover statistically distances via another inversion procedure related to secular parallaxes. Finally, we illustrate the inversion on a fully seven-dimensional epicyclic model. The detailed investigation of this model is postponed to a companion paper (Siebert, Pichon & Bienaymé, in preparation).

2.1 A toy model: parallel sheet model with singular velocity ellipsoid

Let us assume here a sheet-like model for the distribution function of kinematic temperature β:

$$f_\beta(\boldsymbol{r},\boldsymbol{u}) = \sqrt{\frac{\beta}{2\pi}}\exp(-\beta E_z)\delta(v_R)\delta(v_\phi), \tag{4}$$

which corresponds to a stratification in height with a pin-like singular velocity ellipsoid that is aligned with the rotation axis of the Galaxy. Calling $\mu_b \equiv u_b/r$, the energy reads in terms of the heliocentric coordinates

$$E_z = \frac{v_z^2}{2} + \psi_z(z) = \frac{r^2\mu_b^2}{2\cos^2(b)} + \alpha\sin^2(b)r^2 + \chi[r\sin(b)], \tag{5}$$

where the harmonic component of the z potential (αz^2) was made explicit while leaving unspecified the non-harmonic residual, χ.

Putting equation (4) into equation (2) leads to

$$A\ [b,\mu_b,L] = \int\!\!\int \sqrt{\frac{\beta}{2\pi}}\frac{\Phi[Lr^2,\beta]}{\cos(b)} \times \exp\left\{-\beta\alpha r^2\sin^2(b) - \beta r^2\frac{\mu_b^2}{2\cos^2(b)} - \beta\chi[r\sin(b)]\right\} r^3\,\mathrm{d}r\,\mathrm{d}\beta, \tag{6}$$

given the relationship $L_0 = Lr^2$ relating apparent and absolute luminosities. Introducing $\zeta = L^{1/2}r$,

$$x = \alpha\frac{\sin^2(b)}{L} + \frac{\mu_b^2}{2L\cos^2(b)}, \quad \text{and} \quad y = \frac{\sin(b)}{L^{1/2}}. \tag{7}$$

Equation (6) then reads

$$L^2\cos(b)A[b,\mu_b,L] = \int\!\!\int \sqrt{\frac{\beta}{2\pi}}\Phi[\zeta^2,\beta] \times \exp[-\beta\zeta^2 x - \beta\chi(\zeta y)]\zeta^3\,\mathrm{d}\zeta\,\mathrm{d}\beta. \tag{8}$$

2.1.1 Harmonic degeneracy

Suppose for now that the z-potential is purely harmonic, so that χ is identically null. Calling $s = \beta\zeta^2$, the inner integral over ζ in equation (8) can be rewritten as an integral over β and s:

$$\int\!\!\int \sqrt{\frac{\beta}{2\pi}}\Phi[\zeta^2,\beta]\exp(-\beta\zeta^2 x)\zeta^3\,\mathrm{d}\zeta\,\mathrm{d}\beta = \frac{1}{2\sqrt{2\pi}}\int\left(\int \Phi[s/\beta,\beta]\beta^{-3/2}\,\mathrm{d}\beta\right)\exp(-sx)s\,\mathrm{d}s. \tag{9}$$

Equation (9) shows that for a purely harmonic potential the *mixture* of populations (integrated over β) is recovered from $A[b,\ \mu_b,\ L]$, which is effectively a function of x only (given by equation 7). In this instance, the inversion does not allow us to disentangle the different kinematic populations. In physical terms, there is a degeneracy between the distance, luminosity and proper motion. In contrast, when the data set extends far enough to probe the anharmonic part of the potential, we now demonstrate that equation (8) has formally a unique exact solution, before exploring non-parametric means of inverting it in a more general framework.

2.1.2 Uniqueness?

Let us assume that not too far from the Galactic plane, $\chi(z)$ is well approximated by $\chi(z) = \gamma z^\nu$, so that equation (8) becomes

$$L^2\cos(b)A[b,\mu_b,L] = \int\!\!\int \sqrt{\frac{\beta}{2\pi}}\Phi[\zeta^2,\beta] \times \exp(-\beta\zeta^2 x - \beta\gamma\zeta^\nu y^\nu)\zeta^3\,\mathrm{d}\zeta\,\mathrm{d}\beta. \tag{10}$$

Calling

$$\Phi_1[U,B] = \frac{1}{\sqrt{2\pi}}\Phi[\exp(2U),\exp(B)] \times \exp\{4U + 3/2B - c[(2+\nu)U + 2B]\},$$
$$K_0(z) = \exp[cz - \exp(z)], \tag{11}$$

and $$A_1[X,Y] = L^2\cos bA[b,\mu_b,L]\exp[c(X+Y)], \tag{12}$$

where

$$B = \log(\beta), \quad Z = \log(\zeta),$$
$$X = \log(x) = \log\left[\alpha\frac{\sin^2(b)}{L} + \frac{\mu_b^2}{2L\cos^2(b)}\right],$$
$$Y = \log\left|\frac{\gamma\sin^\nu(b)}{L^{\nu/2}}\right|, \tag{13}$$

Equation (10) becomes

$$A_1[b,\mu_b,L] = A_1[X,Y] = \int\!\!\int \Phi_1[Z,B]K_0(B+2Z+X) \times K_0(B+\nu Z+Y)\,\mathrm{d}Z\,\mathrm{d}B. \tag{14}$$

The positive scalar c is left to our discretion and can be chosen so as to yield a narrow kernel, K_0 (in practice, c should be close to one). Since r runs from zero to infinity and so does β, the integration over B and Z will run from $-\infty$ to ∞. Similarly, X and Y span $]-\infty,\infty[$ as b goes from zero to $\pi/2$. Let

$$w = -(B+\nu Z), \quad \varpi = -(B+2Z); \tag{15}$$

Equation (14) then reads

$$A_1[X,Y] = |\nu-2|^{-1}\int\!\!\int \Phi_1[\varpi,w]K_0(X-\varpi) \times K_0(Y-w)\,\mathrm{d}\varpi\,\mathrm{d}w. \tag{16}$$

The *unique* solution of equation (16) reads formally

$$\Phi_1[\varpi,w] = |\nu-2|FT^{-1}\left(\frac{\hat{A}_1[k_\varpi,k_w]}{\hat{K}_0(k_\varpi)\hat{K}_0(k_w)}\right), \tag{17}$$

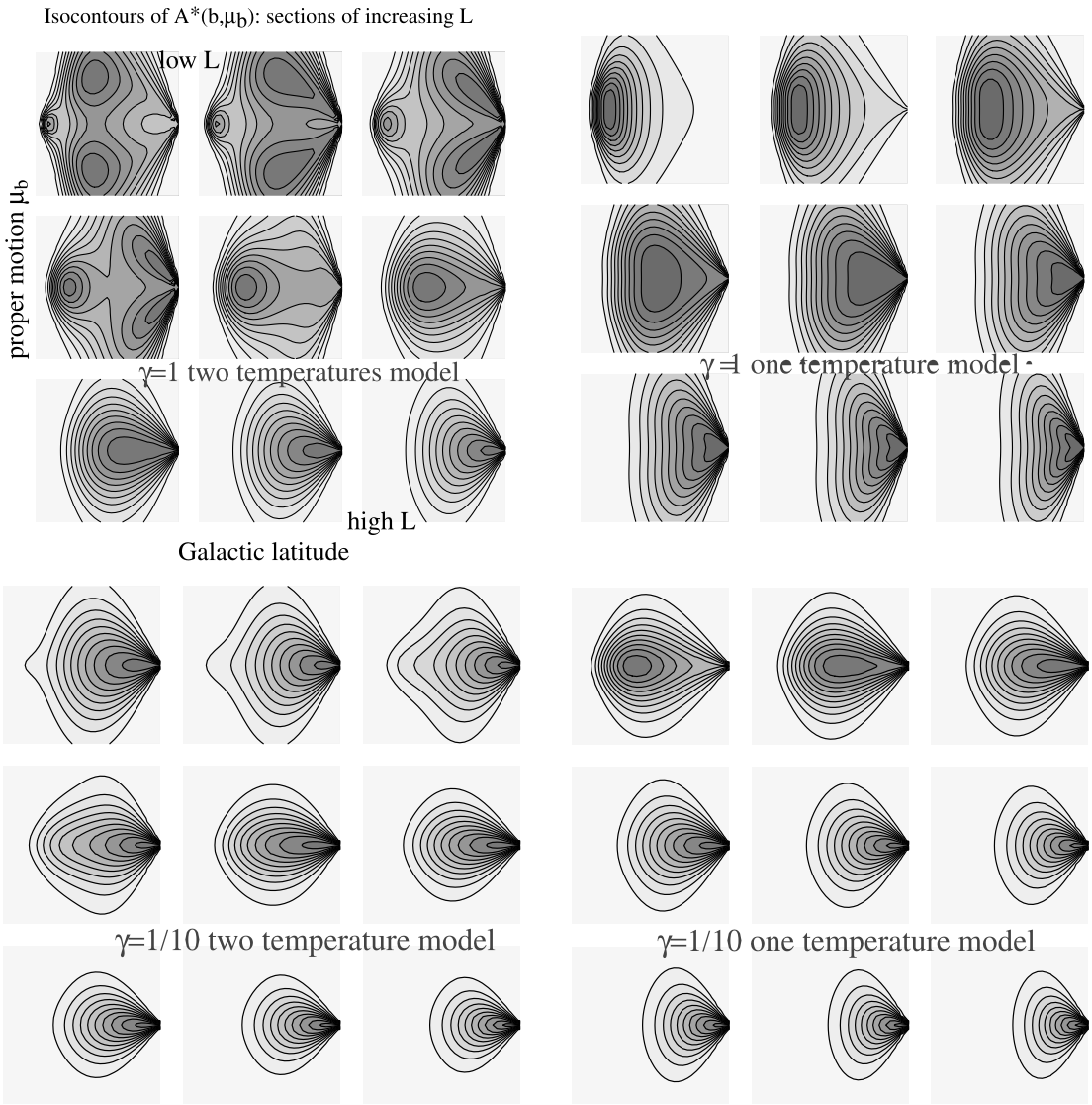

Figure 1. *In each panel:* Isocontour of $A^*(b,\mu_b)$ (defined by equation 48) in the b,μ_b plane (b ranging from $-\pi/2$ to $\pi/2$ and μ_b from -1 to 1): sections of increasing apparent magnitude (from left to right and top to bottom) *Top left:* two-temperature models [$\log\beta = -2$ and $\log\beta = 2$, $\log(L_0) = 0$] *Top right:* same as top left, but for a unique temperature ($\beta = 1$) model. The observed star counts enable us to distinguish between the one- and two-temperature models, especially at the faint end (top left section) for significantly non-zero $\gamma(= 1)$. *Bottom left:* Shows that even the faint end (top left section) of the observed star counts are barely distinguishable from the two-temperature model (*Bottom right:*) for small $\gamma(= 1/10)$. This demonstrates graphically the requirement to access the break radius, $\ell_0 \propto 1/\gamma$, of the potential to derive statistical distances to the stars.

where

$$\hat{A}_1[k_\varpi, k_w] = \int\int \exp[+\mathrm{i}(k_w X + k_\varpi Y)] A_1[X, Y]\,\mathrm{d}X\,\mathrm{d}Y \quad \text{and}$$

$$\hat{K_0}[k] = \int \exp[+\mathrm{i}(kX)] K_0(X)\,\mathrm{d}X,$$

while

$$FT^{-1}[\,f(k_x, k_y)] = \frac{1}{4\pi^2}\int\int \exp[-\mathrm{i}k_x\varpi - \mathrm{i}k_y w] f(k_x, k_y)\,\mathrm{d}k_x\,\mathrm{d}k_y.$$

Both Fourier transforms are well-defined, given the span of ϖ, w and X, Y. Approximating both K_0 and A_1 by a Gaussian of width respectively $1/\ell_K$ and $1/\ell_N^2$, equation (17) shows that Φ_1 will be a Gaussian of width $1/(\ell_N - \ell_K)^2$.

This procedure is therefore a *true* deconvolution: the luminosity function $\Phi_\lambda[L, \beta]$ is effectively recovered at arbitrary resolution (in effect fixed by the signal-to-noise ratio of the data). In practice, equation (17) is impractical for noisy finite data sets, so we shall investigate non-parametric regularized solutions to equation (8) in Section 3.1.1.

There is a natural scale $\ell_0 = (\alpha/\gamma)^{1/(\nu-2)}$, given by the break in the potential, which provides us with a means to lift the degeneracy between faint close stars moving slowly and bright stars moving faster farther out. This scale reflects the fact that statistically the dynamics (i.e., the velocities) gives us a precise indication of distances in units of ℓ_0. We can therefore reassign a posteriori distances to stars in the statistical sense and deconvolve the colour–magnitude diagram. Fig. 1 graphically demonstrates the requirement to access the break radius of the potential in order to derive statistical distances to the stars. It shows sections of increasing apparent magnitude in the b, μ_b plane for a two-temperature model and for a one-temperature model (corresponding to a unique

absolute luminosity). The observed star counts enable us to distinguish between the one- and two-temperature models, especially at the faint end for significantly non-zero γ.

Turning back to equation (8), it remains true that for more general χ the equation can still be inverted in the least-squares sense, but this involves a less symmetric kernel, $K_1(x, y|u, \beta)$, whose functional form depends explicitly on χ:

$$K_1(x, y|u, \beta) = \sqrt{\frac{\beta}{2\pi}} \exp\left[-\beta u^2 x - \beta\chi(uy)\right] u^3.$$

The inversion procedure, which will be described in Section 3, still applies to such kernels.

2.2 A Schwarzschild model: accounting for the local velocity ellipsoid anisotropy

Let us now move to more realistic models with a fully triaxial Schwarzschild ellipsoid. Its distribution function is given in terms of the kinematic inverse dispersions β_R, β_ϕ and β_z by

$$f_\beta(\boldsymbol{r}, \boldsymbol{u}) = \sqrt{\frac{\beta_R \beta_z \beta_\phi}{8\pi^3}} \exp[-(\beta_z E_z + \beta_R E_R + \beta_\phi E_\phi)], \tag{18}$$

where

$$E_z = \tfrac{1}{2} v_z^2 + \psi_z(z), \quad E_R = \tfrac{1}{2} v_R^2 \quad \text{and} \quad E_\phi = \tfrac{1}{2}(v_\phi - \bar{v}_\phi)^2. \tag{19}$$

Here $\bar{v}_\phi$ measures the mean azimuthal velocity in the local neighbourhood (which is assumed not to depend on β), and $\boldsymbol{V} = (v_R, v_\phi, v_z)$ are respectively the radial, azimuthal and vertical velocities of a given star measured in a direct cylindrical system of coordinates centred at the Galactic Centre. These velocities are given as a function of the velocities measured in the frame of the Sun by

$$\begin{aligned} v_\Phi = \frac{1}{R}\{ & r_\odot \sin(b) \sin(\ell) u_b - r_\odot \cos(b) \sin(\ell) u_r - r_\odot \cos(\ell) u_\ell \\ & + r \cos(b)[u_\ell - \sin(\ell) u_\odot] + [r_\odot + r \cos(b) \cos(\ell)] v_\odot \}, \end{aligned} \tag{20}$$

$$\begin{aligned} v_R = \frac{1}{R}\{ & [r \cos(b) - r_\odot \cos(\ell)] \sin(b) u_b - r_\odot \sin(\ell) u_\ell \\ & - \cos(b)[r \cos(b) - r_\odot \cos(\ell)] u_r + r_\odot u_\odot \\ & - r \cos(b) \cos(\ell) u_\odot + r \cos(b) \sin(\ell) v_\odot \}, \end{aligned} \tag{21}$$

$$v_z = \sin(b) u_r + \cos(b) u_b + w_\odot, \tag{22}$$

where

$$R = \sqrt{r_\odot^2 - 2 r_\odot r \cos(b) \cos(\ell) + r^2 \cos(b)^2} \quad \text{and}$$

$$z = r \sin(b). \tag{23}$$

R measures the projected distance (in the meridional plane) to the Galactic Centre, while z is the height of the star. Here $u_\odot, v_\odot, w_\odot$ and $r_\odot$ are respectively the components of the Sun's velocity and its distance to the Galactic Centre. The argument of the exponential in equation (18) is a quadratic function in u_r via equations (20)–(22), so the integration over that unknown velocity component is straightforward.

In short, we show in Appendix A that equation (2) has solutions for families of distributions obeying equation (18). Those solutions are unique, and can be made explicit for a number of particular cases which are discussed there. They are shown to be formally equivalent to those found for equation (4). For instance, at large distances from the Galactic Centre ($r_\odot \to \infty$), equation (6) along the plane $\mu_b = 0$ can be recasted into

$$\begin{aligned} L^2 \cos(b) A_2[b, \ell, \mu_b = 0, L] = & \iint \sqrt{\frac{\beta}{2\pi}} \Phi[u^2, \beta] \\ & \times \exp(-\beta u^2 x_3 - \beta z_2) u^3 \, \mathrm{d}u \, \mathrm{d}\beta, \quad \text{with} \quad x_3 = \alpha \frac{\sin^2(b)}{L}, \end{aligned} \tag{24}$$

and

$$\begin{aligned} z_2 = & \frac{[w_\odot \cos b - (v_\odot - \bar{v}_\phi) \sin b \sin \ell]^2}{2\cos^2(b) + 2\sin^2(b)[\xi_R \cos^2(\ell) + \xi_\phi \sin^2(\ell)]}, \\ \xi_R = & \frac{\beta_z}{\beta_R}, \quad \xi_\phi = \frac{\beta_z}{\beta_\phi}, \end{aligned} \tag{25}$$

which is of the form described in Section 2.1.2 with $\nu = 0$, x_3 replacing x, and z_2 replacing y. With the exception of the special cases also described in Appendix A, the solution can be found via χ^2 minimization, as shown below in Section 3.

2.3 Epicyclic model: accounting for density gradients

The above models do not account for any density or velocity dispersion gradients, which is a serious practical shortcoming. Let us therefore construct an epicyclic model for which the radial variation of the potential and the kinematic properties of the Galaxy are accounted for.

A distribution function solution of Boltzmann equation with two integrals of motion (energy and angular momentum) can be written according to Shu (1969) as

$$f_\beta(\boldsymbol{r}, \boldsymbol{u}) = \Theta(H) \frac{\Omega \beta^{3/2} \rho_D}{\sqrt{2}\pi^{\frac{3}{2}} \kappa \sigma_R^2 \sigma_z} \exp\left(-\beta \frac{E_R - E_\mathrm{c}}{\sigma_R^2} - \beta \frac{E_z}{\sigma_z^2}\right), \tag{26}$$

where Θ is the Heaviside function, while

$$\begin{aligned} \Omega = & \frac{\kappa}{\sqrt{2\alpha + 2}}, \quad \rho_D = \rho_\odot \exp\left(\frac{R_\odot - R_\mathrm{c}}{R_\rho}\right), \quad \text{with} \\ R_\mathrm{c} = & H^{\frac{1}{\alpha+1}} R_\odot^{\frac{\alpha}{\alpha+1}} V_\odot^{-\frac{1}{\alpha+1}}, \end{aligned} \tag{27}$$

α being the slope of the rotation curve, Ω the angular velocity, κ the epicyclic frequency, ρ_D the density, R_c the radius of the circular orbit of angular momentum H, σ_R^2 and σ_z^2 the square of the radial and vertical velocity dispersion, and β the kinematic index

$$\begin{aligned} \sigma_R^2 = & \sigma_{R_\odot}^2 \exp\left(\frac{2R_\odot - 2R_\mathrm{c}}{R_{\sigma_R}}\right), \\ \sigma_z^2 = & \sigma_{z_\odot}^2 \exp\left(\frac{2R_\odot - 2R_\mathrm{c}}{R_{\sigma_z}}\right), \\ E_\mathrm{c} = & \frac{\alpha + 1}{2\alpha} H^{\frac{2\alpha}{\alpha+1}} R_\odot^{-\frac{2\alpha}{\alpha+1}} V_\odot^{\frac{2}{\alpha+1}}. \end{aligned} \tag{28}$$

Here $\rho_0, \Omega, \kappa, \sigma_R, \sigma_z$ and E_c are known functions of momentum H given by

$$\begin{aligned} H = & r_\odot \cos(b) \sin(\ell) u_r - r_\odot \sin(b) \sin(\ell) u_b - [r \cos(b) \\ & - r_\odot \cos(\ell)] u_\ell + r \cos(b) \cos(\ell) u_\odot \\ & + [r_\odot - r \cos(b) \cos(\ell)] v_\odot. \end{aligned} \tag{29}$$

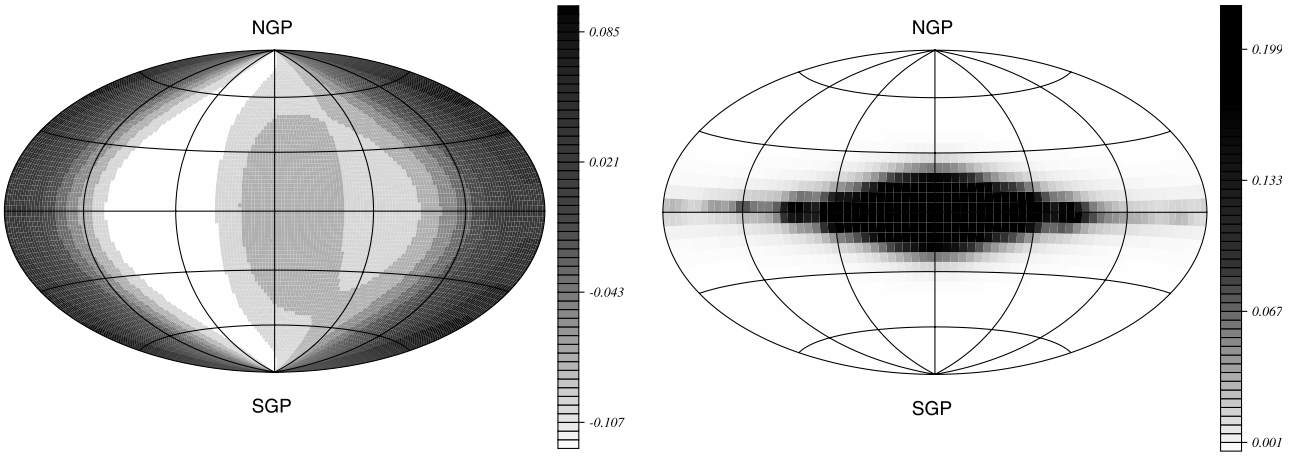

Figure 2. *Left:* Aitoff projection of the normalized density distribution for the epicyclic Shu model. *Right:* Distribution of the maximum of the proper motion along the galactic longitude (in arcsec yr^{-1}). The Galactic Centre is at the centre of the plot, and longitude is increasing from the centre to the left. The asymmetry along the Galactic longitude derives from the peculiar motion of the Sun.

In the case of a separable potential given by

$$\psi(R,z) = \psi_R(R) + \psi_z(z), \quad \text{where} \quad \psi_R(R) = \frac{R^{2\alpha}V_\odot^2 R_\odot^{-2\alpha}}{2\alpha},$$

$$\psi_z(z) = \frac{1}{2\pi G}\left[\Sigma_0\left(\sqrt{z^2+D^2}-D\right) + \rho_{\rm eff} z^2\right], \tag{30}$$

where G is the universal gravity constant, while Σ_0, $\rho_{\rm eff}$ and D are constants, the energies E_z and E_R obey

$$E_z = \frac{[\sin(b)u_r + \cos(b)u_b + w_\odot]^2}{2} + \psi_z(z), \tag{31}$$

$$E_R = \frac{[\cos(b)u_r - \sin(b)u_b]^2 + u_\ell^2 + u_\odot^2 + v_\odot^2}{2} + \psi_R(R) - \sin(\ell)\{u_\ell u_\odot - [\cos(b)u_r - \sin(b)u_b]v_\odot\} + \cos(\ell)\{[\cos(b)u_r - \sin(b)u_b]u_\odot + u_\ell v_\odot\},$$

while R and z are given by

$$R = \sqrt{r_\odot^2 - 2r_\odot r\cos(b)\cos(\ell) + r^2\cos(b)^2} \quad \text{and}$$

$$z = r\sin(b). \tag{33}$$

Note that the integration over u_r in equation (2) must now be carried numerically, since ρ_0, Ω, κ, $\sigma_\parallel$ and σ_z are all functions of u_r via equation (29).

This model, based on the epicyclic theory, accounts for density and velocity dispersion gradients, and is therefore more realistic than the Schwarzschild ellipsoid model presented in Section 2.2. The density distribution together with the distribution of the maximum of the proper motion along the ℓ coordinate are presented in Fig. 2 projected on to the sphere. The asymmetry along the Galactic longitude is produced by the solar motion.

3 SIMULATIONS

3.1 Method

We have chosen to implement a non-parametric inversion technique to invert equation (2) or (8). The non-parametric inversion problem is concerned with finding the best solution to equation (2) or (8) for the underlying LF indexed by kinematic temperature when only discrete and noisy measurements of $[Ab,\ \mu_b,\ L]$ are available (e.g. Titterington 1985; Dejonghe 1993; Lucy 1994; Merritt, 1996; Fadda, Slezak & Bijaoui 1998, Pichon & Thiébaut 1998; and references therein), and most importantly when we have little prejudice regarding what the underlying LF should be. In short, the non-parametric inversion corresponds to model-fitting in a regime where we do not want to impose (say via stellar evolution tracks) what the appropriate parametrization of the model is. It aims at finding the best compromise between noise and bias; in effect, it correlates the parameters so as to provide the smoothest solution amongst all possible solutions compatible with a given likelihood.

An optimal approach should involve a maximum-likelihood solution parametrized in terms of the underlying six-dimensional distribution. In practice, such an approach turns out to be vastly too costly for data sets involving 10^6 measurements. Binning is therefore applied to our ensemble of $(\ell,\ b,\ \mu_\ell,\ \mu_b,\ L,\ B-V)$ measurements.

3.1.1 Non-parametric inversion

The non-parametric solutions of equations (8) and (14) are then described by their projection on to a complete basis of $p\times p$ functions

$$\{e_k(\zeta)e_l(\beta)\}_{k=1,\ldots,pl=1,\ldots,p}$$

of finite (asymptotically zero) support, which could be cubic B-splines (i.e., the unique C^2 function, which is defined to be a cubic over four adjacent intervals and zero outside, with the extra property that it integrates to unity over that interval) or Gaussians:

$$\Phi(\zeta,\beta) = \sum_{k=1}^{p}\sum_{l=1}^{p}\Phi_{kl}e_k(\zeta)e_l(\beta), \tag{34}$$

The parameters to fit are the weights Φ_{kl}. Calling $\mathbf{x} = \{\Phi_{kl}\}_{k=1,\ldots,p,l=1,\ldots,p}$ (the parameters) and $\tilde{\mathbf{y}} = \{L^2\cos(b)\ A(x_i,y_j)\}_{i=1,\ldots,nj=1,\ldots,n}$ (the $n\times n$ measurements, with $L^2\cos(\beta)$ a function of x_i,y_i via equation (7)), equation (8) then becomes

formally

$$\tilde{\mathbf{y}} = \mathbf{a}\cdot\mathbf{x}, \tag{35}$$

where $\mathbf{a}$ is an $(n,n)\times(p,p)$ matrix with entries given by

$$a_{i,j,k,l} = \left\{\int\int e_k(u^2)e_l(\beta)\exp[-\beta u^2 x_i - \beta\chi(uy_j)]u^3\,\mathrm{d}u\,\mathrm{d}\beta\right\}_{i,j,k,l}. \tag{36}$$

For the epicyclic model the measurements are $\tilde{\mathbf{y}} = \{A_{ijklm} = A(\ell_i, b_j, \mu_{\ell_k}\mu_{b_l}, L_m)\}_{i=1,\ldots n_1, j=1,\ldots n_2,, k=1,\ldots n_3,, l=1,\ldots n_4, m=1,\ldots n_5}$ and $\mathbf{a}$ is an $(n_1,n_2,n_3,n_4,n_5)\times(p_1,p_2)$ matrix with entries given by

$$a_{i,j,k,l,m,q,s} = \left\{\int\int\int\int e_q(L_m r^2)e_s(\beta)f_\beta(\ell_i, b_j, \mu_{\ell_k}\mu_{b_l}, r, u_r)r^4 \times \mathrm{d}r\,\mathrm{d}u_r\,\mathrm{d}\beta\right\}_{i,j,k,l,m,q,s}, \tag{37}$$

with f_β given by equation (26).

Assuming that we have access to discrete measurements of A_{ij} (or A_{ijklm} via binning as discussed above), and that the noise in A can be considered to be normal, we can estimate the error between the measured star counts and the non-parametric model by

$$L(\mathbf{x})\equiv\chi^2(\mathbf{x}) = (\tilde{\mathbf{y}} - \mathbf{a}\cdot\mathbf{x})^\perp\cdot\mathbf{W}\cdot(\tilde{\mathbf{y}} - \mathbf{a}\cdot\mathbf{x}), \tag{38}$$

where the weight matrix $\mathbf{W}$ is the inverse of the covariance matrix of the data (which is diagonal for uncorrelated noise, with diagonal elements equal to one over the data variance).

The decomposition in equation (34) typically involves many more parameters than constraints, such that each parameter controls the shape of the function only locally. The inversion problem corresponding to the minimization of equation (38) is known to be ill-conditioned: Poisson noise induced by the very finite sample of stars may produce drastically different solutions, since these solutions are dominated by artefacts due to the amplification of noise. Some trade-off must therefore be found between the level of smoothness imposed on the solution in order to deal with these artefacts on the one hand, and the level of fluctuations consistent with the amount of information in the data set on the other hand. Finding such a balance is called the 'regularization' of the inversion problem, and in effect implies that between two solutions yielding equivalent likelihood, the smoothest is chosen. In short, the solution of equation (35) is found by minimizing the quantity

$$Q(\mathbf{x}) = L(\mathbf{x}) + \lambda R(\mathbf{x}),$$

where $L(\mathbf{x})$ and $R(\mathbf{x})$ are, respectively, the likelihood and regularization terms given by equation (38) and

$$R(\mathbf{x}) = \mathbf{x}^\perp\cdot\mathbf{K}\cdot\mathbf{x}, \tag{39}$$

where $\mathbf{K}$ is a positive definite matrix, which is chosen so that R in equation (39) should be non-zero when $\mathbf{x}$ is strongly varying as a function of its indices. In practice, we use here

$$\mathbf{K} = \mathbf{K_3}\otimes\mathbf{I} + \mathbf{I}\otimes\mathbf{K_3} + 2\mathbf{K_2}\otimes\mathbf{K_2},$$

where $\otimes$ stands for the outer product, $\mathbf{I}$ is the identity matrix, and $\mathbf{K_2} = \mathbf{D_2^\perp}\cdot\mathbf{D_2}$, $\mathbf{K_3} = \mathbf{D_3^\perp}\cdot\mathbf{D_3}$. Here $\mathbf{D}_2$ and $\mathbf{D}_3$ are finite difference second-order operators [of dimensions $(p-2)\times p$ and $(p-3)\times p$ respectively] defined by

$$\mathbf{D}_2 = \mathrm{Diag}_2[-1,2,-1] \equiv \begin{bmatrix} -1 & 2 & -1 & 0 & 0 & \ldots \\ 0 & -1 & 2 & -1 & 0 & \ldots \\ 0 & 0 & -1 & 2 & -1 & \ldots \\ 0 & 0 & 0 & -1 & 2 & \ldots \\ \ldots & \ldots & \ldots & \ldots & \ldots & \ldots \end{bmatrix},$$

$$\mathbf{D}_3 = \mathrm{Diag}_3[1,-3,3,-1] \equiv \begin{bmatrix} 1 & -3 & 3 & -1 & 0 & \ldots \\ 0 & 1 & -3 & 3 & -1 & \ldots \\ 0 & 0 & 1 & -3 & 3 & \ldots \\ 0 & 0 & 0 & 1 & -3 & \ldots \\ \ldots & \ldots & \ldots & \ldots & \ldots & \ldots \end{bmatrix}, \tag{40}$$

This choice corresponds a quadratic operator whose kernel include planes and paraboloids. The operator $\mathbf{K}$ is typically non-zero [and therefore penalizes the minimization of $Q(\mathbf{x})$] for unsmooth solutions (i.e., those leading to strong variations in the coefficients Φ_{kl}).

The Lagrange multiplier $\lambda > 0$ allows us to tune the level of regularization. The introduction of the Lagrange multiplier λ is formally justified by the fact that we want to minimize $Q(\mathbf{x})$, subject to the constraint that $L(\mathbf{x})$ should be in the range $N_{\mathrm{data}} \pm \sqrt{2N_{\mathrm{data}}}$. In practice, the minimum of

$$Q(\mathbf{x}) = (\tilde{\mathbf{y}} - \mathbf{a}\cdot\mathbf{x})^\perp\cdot\mathbf{W}\cdot(\tilde{\mathbf{y}} - \mathbf{a}\cdot\mathbf{x}) + \lambda\mathbf{x}^\perp\cdot\mathbf{K}\cdot\mathbf{x} \tag{41}$$

is

$$\mathbf{x} = (\mathbf{a}^\perp\cdot\mathbf{W}\cdot\mathbf{a} + \lambda\mathbf{K})^{-1}\cdot\mathbf{a}^\perp\cdot\mathbf{W}\cdot\tilde{\mathbf{y}}. \tag{42}$$

The last remaining issue involves setting the level of regularization. The so-called cross-validation method (Wahba 1990) adjusts the value of λ so as to minimize residuals between the data and the prediction derived from the data. Let us define

$$\tilde{\mathbf{a}}(\lambda) = \mathbf{a}\cdot(\mathbf{a}^\perp\cdot\mathbf{W}\cdot\mathbf{a} + \lambda\mathbf{K})^{-1}\cdot\mathbf{a}^\perp\cdot\mathbf{W}. \tag{43}$$

We make use of the value for λ given by generalized cross validation (GCV) (Wahba & Wendelberger 1979) estimator corresponding to the minimum of

$$\lambda_0 \equiv GCV(\lambda) = \min_\lambda\left\{\frac{\|(\mathbf{1} - \tilde{\mathbf{a}})\cdot\tilde{\mathbf{y}}\|^2}{[\mathrm{trace}(\mathbf{1} - \tilde{\mathbf{a}})]^2}\right\}. \tag{44}$$

Note that the model equation (35) is linear and so is equation (42), but this need not be the case when positivity is required. We would then resort to non-linear minimization of equation (41).

3.1.2 *Positivity*

When dealing with noisy data sets, the non-parametric inversion technique presented above (Section 3.1.1) may produce negative coefficients in the reconstructed LF. In order to avoid such effects, positivity can be imposed on those coefficients Φ_{kl} in equation (34). A simple way to achieve positivity is to use an exponential

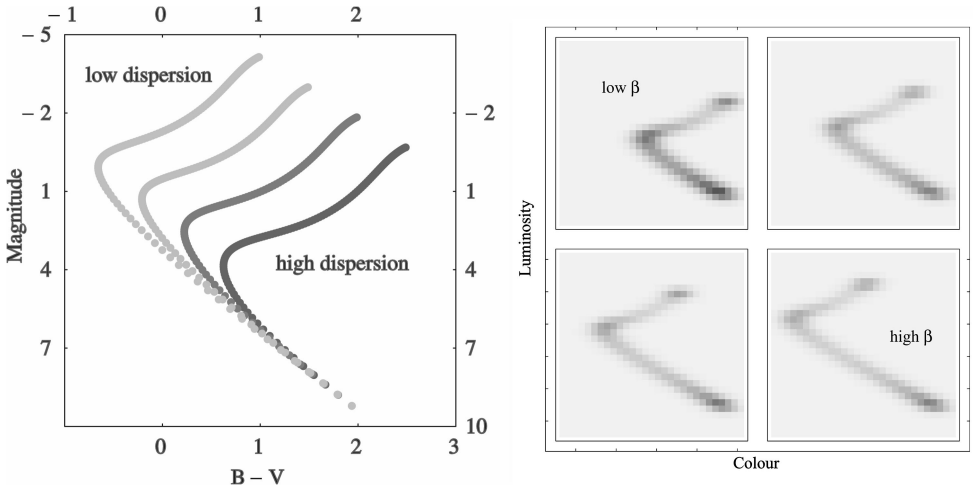

Figure 3. *Left:* Fictitious tracks corresponding to increasing (from left to right) kinematic temperature. *Right:* Decomposition of corresponding colour magnitude diagram into its four components, weighted by the IMF on each track. The image in the observed plane $(\mu_b, b, L, B-V)$ of these tracks is shown in Fig. 4.

transform and introduce φ so that

$$\Phi \equiv \Phi_0 \exp(\varphi), \tag{45}$$

where Φ_0 corresponds to our first guess for Φ (here $\Phi_0 \equiv 10^3$). A first-order Taylor expansion of equation (45), together with equation (35), yields

$$\tilde{\mathbf{y}}' \equiv \tilde{\mathbf{y}} - \mathbf{a}\cdot\Phi_0 = \mathbf{a}\cdot\Phi_0\cdot\varphi \equiv \mathbf{a}\cdot\mathbf{x}', \tag{46}$$

which defines $\tilde{\mathbf{y}}'$ and $\mathbf{x}'$. We first invert equation (46) for $\mathbf{x}'$. The algorithm is then iterative, and we invert in turn for $\mathbf{x}_n'$

$$\tilde{\mathbf{y}}_n' = \mathbf{a}\cdot\mathbf{x}_n', \quad \text{where} \quad \tilde{\mathbf{y}}_n' = \tilde{\mathbf{y}} - \mathbf{a}\cdot\Phi_{n-1} \quad \text{and} \quad \mathbf{x}_n' = \Phi_{n-1}\cdot\varphi_n;$$

the LF is expressed as

$$\Phi_n = \Phi_{n-1}\exp(\eta_{\rm conv}\mathbf{x}_n'/\Phi_{n-1}) \tag{47}$$

in equation (46) for the iteration number n. In practice, convergence is controlled via a parameter, $\eta_{\rm conv} \in [0,1]$, which fixes the amplitude of the correction in equation (47) in order to remain within the régime of the Taylor expansion. It should be emphasized that using equation (46) together with equation (42) (replacing $\mathbf{x}$ by $\mathbf{x}'$) does not lead directly to the expected LF but to a correction that has to be applied to Φ_0.

We will now proceed to invert equation (10) in two régimes: the Schwarzschild model described by equation (18), and the epicyclic model given by equation (26). The former model is dimensionally less demanding, while the latter is more realistic, since it accounts for density and velocity dipsertion gradients.

3.2 Simulated Schwarzschild models

We will first focus on the inversion of equation (8), rather than (A5) or (A8) (which were shown to be equivalent in the zero asymmetric drift approximation) and (24) (which was also shown to be of the same form). Special emphasis is put on the toy model described in Section 2.1 while carrying the inversion on a superposition of four kinematically decoupled populations with distinct main sequence turn-off magnitudes. These are illustrated in Fig. 3, which displays the four fictitious tracks corresponding to increasing kinematic temperature weighted by some IMF on each track. The image in the observed plane $(\mu_b, b, L, B-V)$ of these tracks is shown in Fig. 4, which shows isocontours of A^* defined by (corresponding to equation 12 with $c = 3/4$)

$$A^*[b,\mu_b,L] = A[b,\mu_b,L]\cos(b) \times \left\{\frac{\gamma\sin^{\nu}(b)[\mu_b^2\sec^2(b) + 2\alpha\sin^2(b)]}{2L^{\nu/2-5/3}}\right\}^{3/4} \tag{48}$$

in the b,μ_b plane for increasing $B-V$ at a fixed apparent magnitude $L = 1/10$. The multiple kinematic components of the redder sections display distinct extrema for opposite values of μ_b at fixed Galactic latitude, b, and also as a function of b at fixed proper motions. In all figures, γ is chosen equal to 1 (unless specified

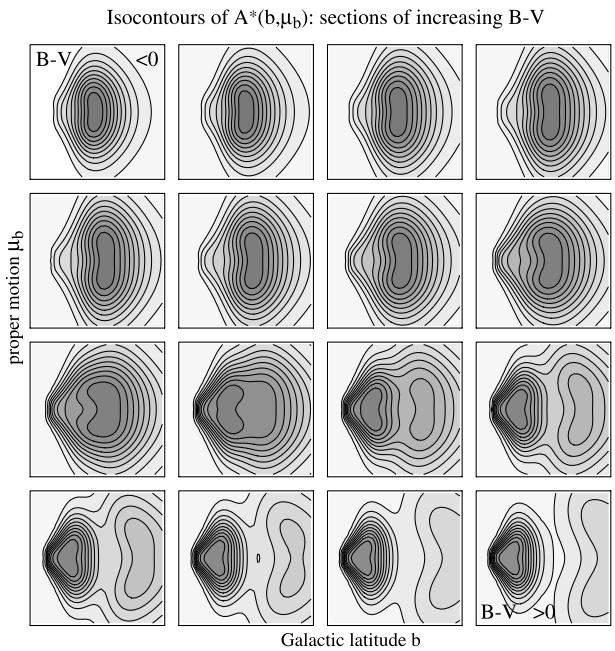

Figure 4. $A^*(b,\mu_b,B-V)$ in the b,μ_b plane for increasing $B-V$ (from left to right and top to bottom) at a fixed apparent magnitude $L = 1/10$ of the model described in Fig. 3. Interestingly, the multiple kinematic components of the redder sections display distinct extrema for opposite values of μ_b at fixed Galactic latitude, b, and also as a function of b at fixed proper motions.

Table 1. Parameters used for the epicyclic model described in Section 2.3.

Distribution function	Potential	Solar motion
$R_\rho = 2.5$ kpc	$D = 240$ pc	$R_\odot = 8.5$ kpc
$R_\rho = 2.5$ kpc	$\Sigma_0 = 48\,\mathrm{M}_\odot\,\mathrm{pc}^{-2}$	$V_{\rm LSR} = 220\,\mathrm{km\,s}^{-1}$
$R_{\sigma_R} = 10$ kpc	$\rho_{\rm eff} = 0.0105\,\mathrm{M}_\odot\,\mathrm{pc}^{-3}$	$U_\odot = 9\,\mathrm{km\,s}^{-1}$
$R_{\sigma_z} = 5$ kpc	$\alpha = -0.1$	$V_\odot = 5.2\,\mathrm{km\,s}^{-1}$
$\sigma_{R_\odot} = 48\,\mathrm{km\,s}^{-1}$		$W_\odot = 7\,\mathrm{km\,s}^{-1}$
$\sigma_{z_\odot} = 24\,\mathrm{km\,s}^{-1}$		
$\rho_\odot = 0.081\,\mathrm{M}_\odot\,\mathrm{pc}^{-3}$		

otherwise) and ν equal to 3. For simplicity, we also numerically approximate K_0 in equation (11) by a Gaussian, since the matrix elements in equation (37) are then analytic.

3.3 Simulated epicyclic models

In order to test the inversion procedure, a set of four HR diagrams with different turn-off luminosity was constructed, assuming a mass–luminosity relation (MLR) and a Salpeter initial mass function (IMF). The LF of each population scales like

$$\Phi_0 \propto L^{-\frac{\sigma}{\tau}}, \tag{49}$$

where τ (the slope of the MLR on a logarithmic scale) was set to 3.2, which is characteristic of the main sequence, and σ to 2.35 (the IMF slope). The scaling factor fixes the number of stars in the simulated galaxy. The tracks associated with those HR diagrams were then binned on a $20 \times 20 \times 4$ grid in the $[L_0, B-V, \mathit{beta}]$ space; those HR diagrams represent the absolute luminosity function, $\Phi_{B-V}(L_0, \beta)$. The *observed* counts were then computed assuming that each track corresponds to a given kinematic index, and that its distribution can be reproduced by the epicyclic model of the same kinematic index, i.e.,

$$\mathrm{d}N\,(\ell_i, b_j, \mu_{\ell,k}, \mu_{b,l}, L_m, B-V) = a_{i,j,k,l,m,q,s} \times [\Phi_0(B-V)]_{q,s}\,\mathrm{d}\mu_\ell\,\mathrm{d}\mu_b\,\mathrm{d}\ell\cos b\,\mathrm{d}b\,\mathrm{d}L\,\mathrm{d}(B-V), \tag{50}$$

where $a_{i,j,k,l,m,q,s}$ is given by equation (37). Poisson noise was introduced in corresponding histograms used as input for the inversion procedure. It should be emphasized that constructing such HR diagrams does not challenge the relevance of our physical model, equation (26), but only our ability to recover a given LF. The model LF need not be very realistic at this stage. The parameters of the epicyclic model given in Table 1 were set so as to reproduce the local neighbourhood according to Bienaymé & Séchaud (1997) and Vergely et al. (2001). Fig. 8 shows the assumed and reconstructed HR diagrams for the four populations in the $[L_0, B-V]$ plane for this model, while Fig. 9 shows the reconstruction error in per cent for those two figures.

4 RESULTS

4.1 The Schwarzschild models

The above non-parametric inversion technique was implemented on $19 \times 19 \times 19$ data sets (and up to $41 \times 41 \times 41$) corresponding to measurements in $X, Y, B-V$ (equation 13). For each $B-V$ section, we recover 19×19 (respectively 41×41) coefficients $\mathbf{x}_{ij}$ corresponding to values of U,B, which implies that our resolution in kinematic dispersion is logarithmic. Fig. 5 shows isocontours of the assumed and reconstructed HR diagram as its decomposition in kinematic dispersion. In this zero-noise, no-bias régime, the relative discrepancy between the data and the projection of the model is less than one part in 10^3, while that between the model and the inversion is lower than 10 per cent (the corresponding loss in accuracy is characteristic of non-parametric deconvolution). Note that the wiggly structures are a property of the model, and are well recovered by the inversion procedure. Fig. 6 shows the actual deprojection overlaid on top of the expected contour of the model in the (logarithmic) (β, L) plane for increasing values of $B-V$ (the projection of the fit in data space is not displayed, because residuals of the fit would be too small to be seen). Errors in the deprojection are largest for lower contours. Note that the contours in Fig. 5 correspond to sections of the cube shown in Fig. 6 that are orthogonal to those displayed in Fig. 6.

4.1.1 Errors in measurements and finite sample

The above results were achieved assuming infinite numbers of stars and no truncation in apparent magnitude. The Poisson noise induced by the finite number of stars (for which accurate photometric and kinematic data are available), as well as the actual error in those measurements, are likely to make the inversion of equation (8) troublesome.

Fig. 7 shows how the error in the recovered HR diagram decreases as a function of the signal-to-noise ratio in the data which, for the sake of simplicity, was assumed to be constant while the noise was taken to be Gaussian (corresponding to the large number of stars per bin). Note that in reality the signal-to-noise ratio will clearly be apparent-magnitude-dependent, and distance-dependent (because of extinction and proper motion errors). Fig. 7 also shows how the truncation in apparent magnitude induces a truncation in absolute magnitude (here we truncate in Y, since a truncation in L induces a truncation in Y but none in X, given equation 13).

4.2 The epicyclic models

The inversion technique has been implemented over a $36 \times 9 \times 7 \times 7 \times 10 \times 20 \times 4$ model which corresponds to a bin size projected on to the sphere of 10×10 degrees in position sampled linearly, seven bins in proper motion ranging from -0.2 to $0.2\,\mathrm{mas\,yr}^{-1}$, and 20 bins in apparent and absolute luminosity corresponding to an integration over the line of sight from 0.1 pc to 4 kpc (those are also linear bins in luminosity, which correspond to a logarithmic binning in radius). The four kinematic indexes (ranging from 0.8 to 120) were set to reproduce a series of discs with density scaleheights ranging from nearly 200 pc to 1 kpc (i.e., corresponding to thin and thick discs). The mean signal-to-noise ration for these simulation is 2000, ranging from 20 on the giant branches to 70 000 at the bottom of the main sequence.

Fig. 9 shows the reconstruction error in the $[B-V, L_0]$ plane corresponding to the HR diagram shown in Fig. 8. The main sequence and the different turn-off are well reconstructed (the error lies well below 1 per cent for the faint part of the main sequence, and is less than 10 per cent at the turn-offs). The red giant branch (RGB) is also well reproduced, even though it strongly depends on the age of the population (via β). This can be understood if we look at the number of stars in the different regions on the $[B-V, L_0]$ plane. Older (younger) populations have larger (lower) number of stars on the RGB, and the signal-to-noise ratio is increasing (decreasing) correspondingly. We note that the four tracks are recovered without creating any spurious structure. The LFs $\Phi_\beta(L_0)$

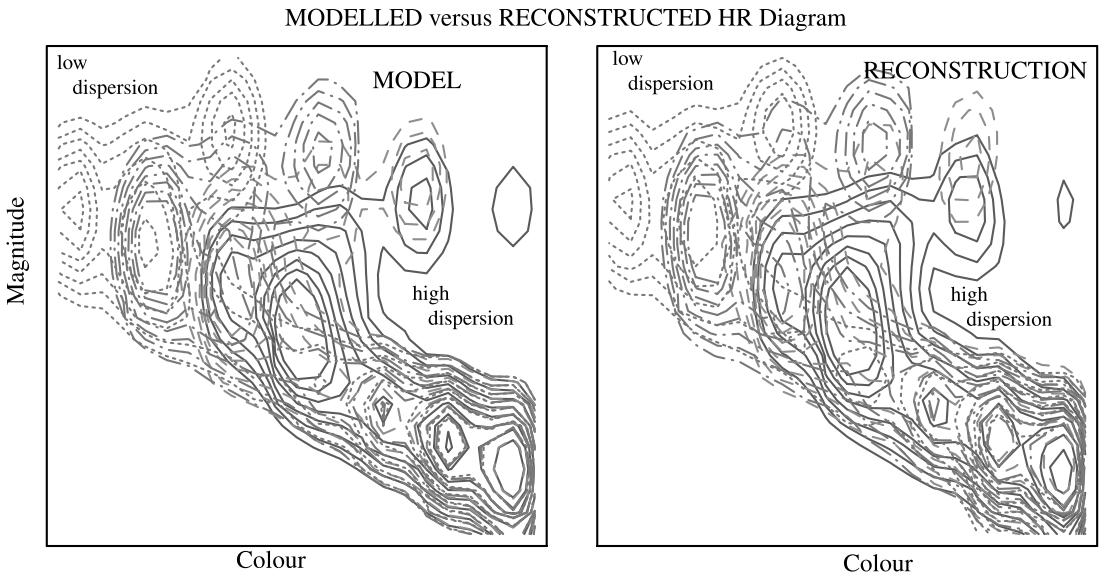

Figure 5. *Left:* assumed and *Right:* reconstructed HR diagram together with its decomposition in kinematic temperature. Note that the wiggly structures are a property of the model, and are well recovered by the inversion procedure. The plain, dashed, dot-dashed, short-dashed curves correspond to the four dispersions associated with the four populations with distinct main-sequence turn-off radii shown in Fig. 3.

are recovered within 1 per cent uncertainty (in mean value) for the oldest population, and within 20 per cent for the youngest (note that sometimes the reconstruction error increases up to 100 per cent when no stars are recovered on the RGB).

5 DISCUSSION AND CONCLUSION

The main result of this paper is a demonstration that the generalized stellar statistic equation including proper motions, equation (2), can be inverted, giving access to both the kinematics and the luminosity function. The inversion was carried for two rather specific functional decompositions of the underlying distribution (namely, constant ratio and possibly singular Schwarzschild ellipsoids plane-parallel models) and a more realistic physical model (the epicyclic Shu model) which accounts for gradients. The inversion assumes that the departure from harmonicity of the vertical potential, and/or the asymmetric drift or the Sun's vertical velocity, $w_\odot$, are known. Indeed, the break in the potential yields a scale which reflects the fact that statistically the dynamics (i.e., the velocities) gives a precise indication of distances in units of that scale. The asymmetric drift or vertical component of the Sun's velocity provides another energy scale (and therefore a distance scale). The existence of more than one distance scale is mathematically redundant, but practically of interest for the purpose of accounting for local and remote stars.

In a nutshell, it was shown in Section 2 that equation (2) has solutions for families of distributions obeying equation (4) (singular ellipsoid) or equation (18) (Schwarzschild ellipsoid). Those solutions are unique, and can be made explicit for a number of particular cases: equation (17) (pin-like velocity ellipsoid), equation (A5) (constant ratio β_R/β_z, $w_\odot \approx 0$), equation (A8) (constant ratio β_R/β_z and β_ϕ/β_z, either with $v_\odot \approx \bar{v}_\phi, w_\odot \approx 0$, or with $v_\odot - \bar{v}_\phi \neq 0$, $w_\odot \neq 0$ and $\chi \approx 0$: statistical secular parallaxes). In all other instances, the solution can be found via the general non-parametric inversion procedure described in Section 3.1.1, the only constraint being the computation of the model matrix generalizing equation (37) (which might require numerical integration, as shown for instance in Section 2.3); in this more general framework it remains also to demonstrate that the inversion will converge towards a solution which is *unique*. For instance, in the régime where the epicyclic model has been tested (Section 3.3) a unique solution seems to be well defined. The LF of each kinematical component is well recovered throughout the HR diagram.

More tests are required before applying the method to real data, and are postponed to a companion paper (Siebert et al., in preparation). For a given vertical potential, it appears that the modelling of star counts indexed by proper motion $A_\lambda(m, \mu_l, \mu_b;$

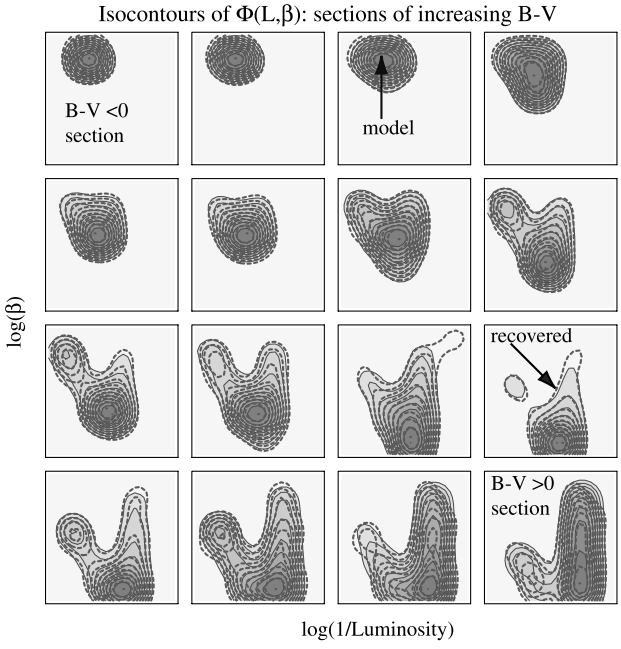

Figure 6. Assumed model (plain line, filled contour) and non-parametric deprojection (dashed line) overlaid on top of the expected contours in the $(\log 1/L,\ \log \beta)$ plane for increasing $B-V$ sections. Errors in the deprojection are largest for lower contours. Note that these sections are orthogonal to those superposed in Fig. 5.

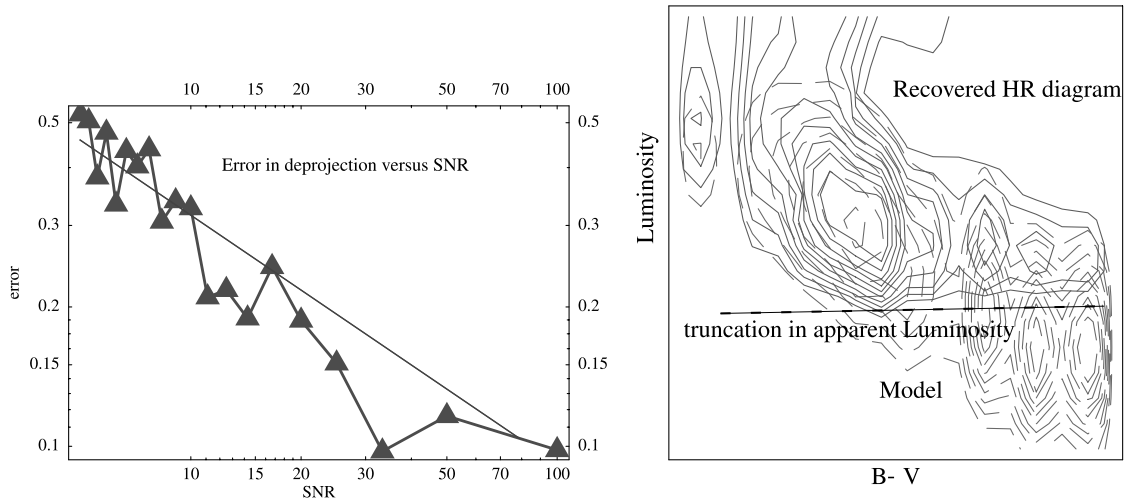

Figure 7. *Left panel:* The mean absolute residual of the luminosity function, $\sum_{ij}|\Phi_{ij}^{\rm recov} - \Phi_{ij}^{\rm input}|/\sum_{ij}|\Phi_{ij}^{\rm input}|$ versus the signal-to-noise ratio in logarithmic coordinates. This graph demonstrates that the non-parametric inversion sketched in Section 3.1.1 is robust with respect to sampling or measurement noise. *Right panel:* The effect of truncation in magnitude on the main sequence: plain line: recovered HR diagram with a truncated data set; dashed line: recovered HR diagram without truncation. As expected, the truncation in apparent magnitude removes the information at the bottom of the main sequence.

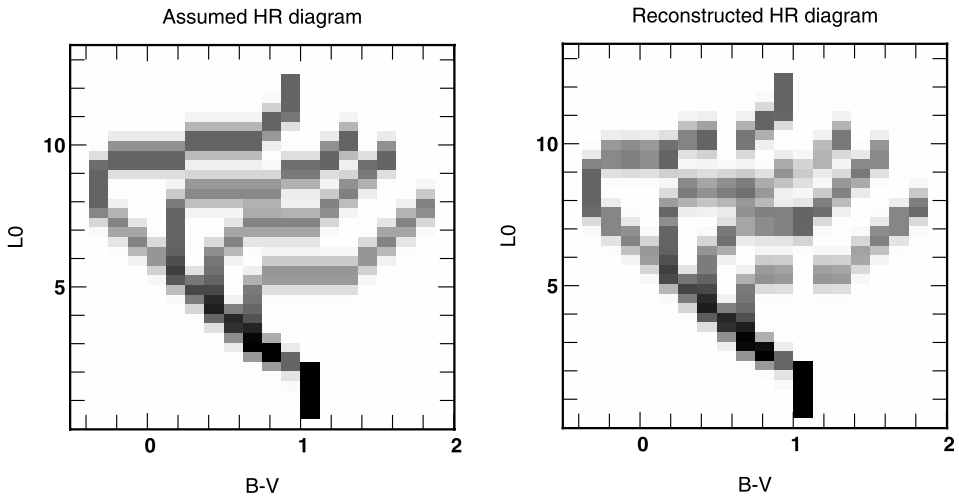

Figure 8. *Left:* Assumed HR diagram for the epicyclic model. The four populations have distinct turn-off point and kinematic index. *Right:* Reconstructed HR diagram. L_0 is expressed in unit of $L_\odot$. Note that all four populations are well recovered. The main sequence and turn-off are reconstructed within 10 per cent error (less than 1 per cent for the lower part of the main sequence due to the large number of stars in that part of the HR diagram). The giant branch is also recovered, although the reconstruction error is higher.

l, b) has a solution for most model parameters. Many different models based on distinct *priors* have produced realistic magnitude and colour star counts, but failed to predict proper motion measurements accurately [for instance, note that the Besançon model – which relies on a nearly dynamical consistent model – produces a good fit to proper motion surveys (Ojha et al. 1994), while dynamically inconsistent models are more problematic (Ratnatunga, Bahcall & Casertano 1989)].

It should be emphasized that the inversion method presented in Section 3.1.1 is a true deconvolution, and should give access to a kinematically indexed HR diagram. Together with some model of the time evolution of the different kinematic components (via, say, a disc-heating mechanism), the indexing could be translated into one on a cosmological time, hence providing a non-parametric measurement of the local neighbourhood LF which is complementary to that obtained by evolutionary track fitting with an assumed IMF and star formation rate (see, e.g., Hernandez, Valls-Gabaud & Gilmore 1999). Note that, conversely, the agreement between the standard direct method to predict the local LF and the method presented here could be used to measure the Galactic potential.

The deepest photometric and proper motion of whole sky survey available is the Tycho-2 catalogue (Høg et al. 2000), which is a new reduction of the Tycho data (Høg et al. 1998). Many Tycho stars are disc giants and subgiants covering a large range of distances; the method developed here can be applied to these stars, and will allow us to recover their LF without any prior information from stellar evolution tracks. We intend in a forthcoming paper to apply the method presented here to the Tycho-2 catalogue (Høg et al. 1998) and to other proper motion catalogues in order to determine the LF of stars in the solar neighbourhood. We will investigate the limitations introduced by a magnitude-limited catalogue, by the finite size of catalogues, and also by our limited knowledge of the Galactic potential. Reddening is also bound to be a concern, since it will bias apparent luminosities as a function of ℓ and b. If

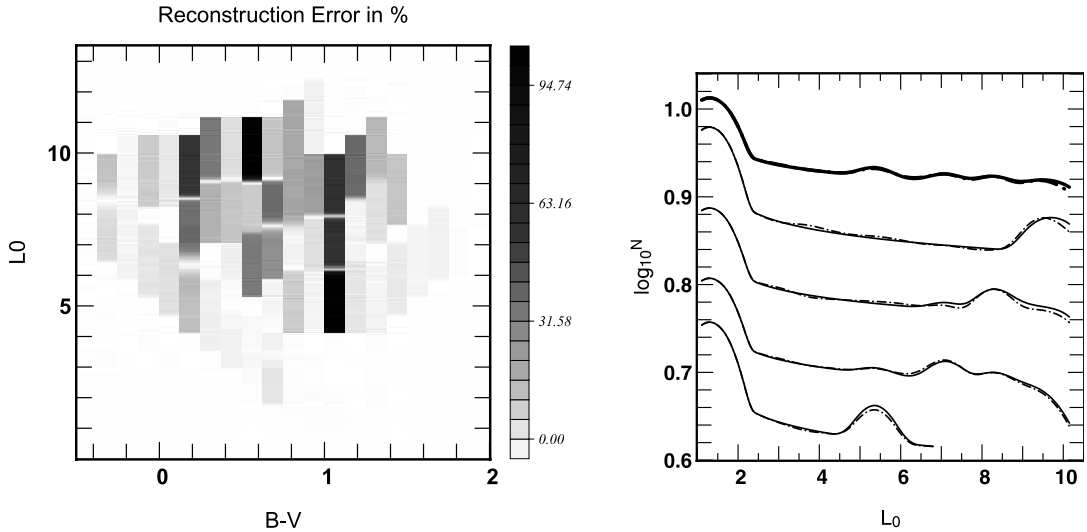

Figure 9. *Left panel:* Reconstruction error in the $[B-V, L_0]$ plane for the epicyclic model shown in Fig. 8. *Right panel:* Model versus recovered luminosity function $\Phi_\beta(L_0)$ for the four kinematic indexes corresponding to the oldest population (lower curve) to the youngest (upper curve). The LFs are plotted on a logarithmic scale and arbitrary normalized. The curves corresponding to the two kinematic index where shifted along the *y*-axis. Plain lines correspond to the model LF, while dot-dashed lines are the reconstructed LF. Note that the LF is well reconstructed for the main sequence (at low luminosity) and for the turn-off. The total LF summed over the kinematic index is also displayed as the top thick lines. The bumps at low and high luminosity are properties of the model and correspond to the lower part of the main sequence and to the subgiant branch of each population.

the reddening is diffuse and the absorbing component law is known, the kernel of e.g., equation (10) will simply be modified accordingly. Alternatively, multicolour photometry could be sufficient to constrain the spatial extinction law. Of course, the dimensionality of the problem is increased by the number of colour bands used, since the analysis must be carried while accounting for all colours simultaneously.

The final error on the recovered LFs will depend on the photometric errors of the observational catalogue (~ 0.1 for the Tycho-2 catalogue down to 0.013 for $V_T < 9$, ~ 0.05–0.10 for photographic surveys). It will also depend on the relative proper motion accuracy [$\delta(m) \sim 2\delta(\mu)/\sigma_\mu$, with σ_μ the typical dispersion for a stellar group at a given distances]. With the Tycho-2 catalogue completed by proper motions (with an accuracy of 2.5 mas y^{-1}), and for disc giants with velocity dispersions from 10 to 50 km s^{-1} and proper motion dispersions from 2 to 10 mas y^{-1}, the accuracy on the recovered LF will be limited to about 0.5 mag. Closer (and fainter) stars with proper motions from photographic catalogues will constrain the lower part of the LF with a higher accuracy.

In the next decade, sky surveys by the *Fame*, *Diva* and *GAIA* satellites will probe the Galactic structure in superb detail, giving directly access to larger volumes of the 6D stellar phase space of the Galaxy. It will remain that farther out, only proper motions and photometry will have sufficient accuracy and generalization of methods such as that derived here will be used to extrapolate our knowledge of the kinematic and LFs of the Galaxy and its satellites. For instance, Appendix B sketches the possible inversion of an external globular cluster LF with *GAIA*-quality photometry.

ACKNOWLEDGMENTS

We thank J. L. Vergely for early stimulating discussions on this project, and E. Thiébaut for fruitful comments.

REFERENCES

Bahcall J. N., Soneira R. M., Schmidt M., 1983, ApJ, 265, 730
Bienaymé O., Séchaud N., 1997, A&A, 323, 781
Binney J., Merrifield M., 1998, Galactic Astronomy. Princeton Series in Astronomy, Princeton Univ. Press, Princeton
Bok B. J., 1937, The Distribution of Stars in Space. Univ. Chicago Press, Chicago
Buser R., Kaeser U., 1985, A&A, 145, 1
Dejonghe H., 1993, in Dejonghe H., Habing H. J., eds, Proc. IAU Symp. 153, Galactic Bulges. Kluwer, Dordrecht, p. 73
Fadda D., Slezak E., Bijaoui A., 1998, A&AS, 127, 335
Gould A., Flynn C., Bahcall J. N., 1998, ApJ, 508, 798
Haywood M., Robin A. C., Crézé M., 1997a, A&A, 320, 428
Haywood M., Robin A. C., Crézé M., 1997b, A&A, 320, 444
Hernandez X., Valls-Gabaud D., Gilmore G., 1999, MNRAS, 304, 705
Høg E., Kuzmin A., Bastian U., Fabricius C., Kuimov K., 1998, A&A, 335, L65
Høg E. et al., 2000, A&A, 355, L27
Lucy L., 1994, A&A, 289, 983
Merritt D., 1996, AJ, 112, 1085
Mihalas D., Binney J., 1981, Galactic Astronomy: Structure and Kinematics. W. H. Freeman & Company
Ojha D. K., Bienaymé O., Robin A. C., Mohan V., 1994, A&A, 290, 771
Pichon C., Thiébaut E., 1998, MNRAS, 301, 419
Pritchet C., 1983, AJ, 88, 1476
Ratnatunga K. U., Bahcall J. N., Casertano S., 1989, ApJ, 339, 106
Reid I. N., Yan L., Majewski S., Thompson I., Smail I., 1996, AJ, 112, 1472
Robin A., Crézé M., 1986, A&AS, 64, 53
Shu F. H., 1969, ApJ, 158, 505
Titterington D. M., 1985, A&A, 144, 381
Vergely J.-L., Egret D., Köeppen J., Bienaymé O., 2001, A&A, submitted
von Seeliger H. H., 1898, Abh. K. Bayer Akad Wiss Ser II Kl, 19, 564
Wahba G., 1990, Spline models for Observational Data. CBMS-NSF Regional Conf. Ser. App. Mathematics Soc. Industrial and Applied Mathematics, Philadelphia
Wahba G., Wendelberger J., 1979, Monthly Weather Review, 108, 1122

APPENDIX A: ASYMPTOTIC ANALYTIC SOLUTIONS FOR THE SCHWARZSCHILD MODEL

Let us demonstrate that equation (2) has explicit analytic solutions

for families of distributions obeying (18), using the inversion procedure sketched in Section 2.1.

A1 Slices towards the Galactic Centre

For the sake of simplicity, let us first restrict the analysis to $u_\odot = v_\odot = w_\odot = 0$ and assume first that we have measurements only in the direction $\ell = 0$. The integration over u_r then yields

$$\int f_\beta(\boldsymbol{r},\boldsymbol{u})\,\mathrm{d}u_r = \sqrt{\frac{\beta_b\beta_\phi}{4\pi^2}} \times \exp\{-\tfrac{1}{2}[\beta_\phi(u_\ell - \bar{v}_\phi)^2 + \beta_b u_b^2] - \beta_z\psi_z(z)\}, \tag{A1}$$

where

$$\beta_b^{-1} = \beta_R^{-1}\sin^2(b) + \left[\frac{r_\odot - r\cos(b)}{R}\right]^2 \beta_z^{-1}\cos^2(b). \tag{A2}$$

Without loss of generality, let us integrate over u_ℓ:

$$\iint f_\beta(\boldsymbol{r},\boldsymbol{u})\,\mathrm{d}u_r\,\mathrm{d}u_\ell = \sqrt{\frac{\beta_b}{2\pi}}\exp[-\tfrac{1}{2}\beta_b u_b^2 - \beta_z\psi_z(z)]. \tag{A3}$$

At large distances from the Galactic Centre, both R and $r_\odot$ are large compared to r, and equation (A2) becomes

$$\bar{\beta}_b^{-1} = \beta_R^{-1}\sin^2(b) + \beta_z^{-1}\cos^2(b). \tag{A4}$$

Let us now also assume that β_R and β_z are known monotonic functions of a unique parameter β. We may now convolve equation (A3) with the LF sought, $\Phi[Lr^2,\beta]$, so that

$$A[b,\mu_b,L] = \iint\sqrt{\frac{\bar{\beta}_b}{2\pi}}\Phi[Lr^2,\beta] \times \exp\{-\tfrac{1}{2}r^2\bar{\beta}_b\mu_b^2 - \beta_z\psi_z[r\sin(b)]\}r^3\,\mathrm{d}r\,\mathrm{d}\beta. \tag{A5}$$

Equation (6) appears now as a special case of equations (A4) and (A5) corresponding to $\beta_R\rightarrow\infty$. Even though the convolution in equation (A5) is less straightforward than that of equation (8), and so long as ψ_z is not purely harmonic, equation (A5) will have a non-trivial solution for Φ. In particular, if the ratio of velocity dispersions β_R/β_z is assumed constant, equation (8) still holds but with $\beta = \beta_z$, and x replaced by x' defined by

$$x' = \alpha\frac{\sin^2(b)}{L} + \frac{\mu_b^2}{2L\cos^2(b) + \xi 2L\sin^2(b)}, \quad \text{where} \quad \xi = \frac{\beta_z}{\beta_R},$$

$$\text{with} \quad A'[b,\mu_b,L] = A[b,\mu_b,L]\sqrt{1+\xi\tan^2(b)}.$$

Note that if $v_\odot$ and $w_\odot$ are not negligible, equation (A5) becomes

$$A[b,\mu_b,L] = \iint\sqrt{\frac{\bar{\beta}_b}{2\pi}}\Phi[Lr^2,\beta]\exp\{-\tfrac{1}{2}\bar{\beta}_b[u_b + \cos(b)w_\odot]^2 - \beta_z\psi_z[r\sin(b)]\}r^3\,\mathrm{d}r\,\mathrm{d}\beta, \tag{A6}$$

and is of the form discussed below as equation (A8) with $\ell = 0$.

A2 Slices away from the Galactic Centre

For any direction $\ell \neq 0$ when $r_\odot\rightarrow\infty$, the kinetic dispersion (replacing in equation A4) along Galactic latitude is given by

$$\hat{\beta}_b^{-1} = (\beta_R^{-1}\cos^2\ell + \beta_\Phi^{-1}\sin^2\ell)\sin^2 b + \beta_z^{-1}\cos^2 b,$$

and equation (6) is replaced by

$$A\ [b,\ell,\mu_b,L] = \iint\sqrt{\frac{\hat{\beta}_b}{2\pi}}\Phi[Lr^2,\beta]\exp\{-\hat{\beta}_b[r\mu_b + \cos(b)w_\odot - \sin(b)\sin(l)(v_\odot - \bar{v}_\phi)]^2 - \beta_z\psi_z[r\sin(b)r^3\,\mathrm{d}r\,\mathrm{d}\beta]\}, \tag{A7}$$

which can be rearranged as (again with $\beta = \beta_z$)

$$L^2\cos(b)A_2[b,\ell,\mu_b,L] = \iint\sqrt{\frac{\beta}{2\pi}}\Phi[u^2,\beta] \times \exp[-\beta u^2 x_2 + \beta u y_2 - \beta z_2 - \beta\chi(uy)]u^3\,\mathrm{d}u\,\mathrm{d}\beta, \tag{A8}$$

with z_2 given by equation (25),

$$x_2 = \alpha\frac{\sin^2(b)}{L} + \frac{\mu_b^2}{2L\cos^2(b) + 2L\sin^2(b)[\xi_R\cos^2(\ell) + \xi_\phi\sin^2(\ell)]}, \tag{A9}$$

$$y_2 = \frac{\mu_b[(v_\odot - \bar{v}_\phi)\sin b\sin\ell - w_\odot\cos b]}{\sqrt{L}\cos^2(b) + \sqrt{L}\sin^2(b)[\xi_R\cos^2(\ell) + \xi_\phi\sin^2(\ell)]}, \tag{A10}$$

$$A_2[b,\ell,\mu_b,L] = A[b,\mu_b,L] \times\sqrt{1 + \tan^2(b)[\xi_R\cos^2(\ell) + \xi_\phi\sin^2(\ell)]},$$

$$\text{where} \quad \xi_R = \frac{\beta_z}{\beta_R}, \quad \xi_\phi = \frac{\beta_z}{\beta_\phi}. \tag{A11}$$

In the region where the asymmetric drift and the z-component of the Sun's velocity can be neglected, $v_\odot \approx \bar{v}_\phi$ and $w_\odot \approx 0$, y_2 and z_2 vanish and equation (A8) is formally identical to equation (10); once again the solution of equation (A8) is given by equation (17) with the appropriate substitutions. Alternatively, in the regions where either $w_\odot$ or $v_\odot - \bar{v}_\phi$ cannot be neglected, equation (A8) has a unique solution even if $\chi \equiv 0$, which can be found along the section $\mu_b = 0$ (note that when $r_\odot\rightarrow\infty$, we can always assume $u_\odot = 0$ by changing the origin of Galactic longitude, ℓ). Indeed, equation (A8) becomes equation (24), which is of the form described in Section 2.1.2 with $\nu = 0$, x_3 replacing x, and z_2 replacing y; the corresponding solution is found by following the same route. It is analogous to statistical secular parallaxes (note, none the less, that the section $\mu_b = 0$ might not be sufficient to carry the inversion without any truncation bias, since $\log(z_2)$ spans $]-\infty,Z[$ when b and ℓ vary with Z as a function of ξ_R, ξ_Φ, $w_\odot$ and $(v_\odot - \bar{v}_\phi)$.

Turning back to equation (A8), it remains true that for more general χ the equation can still be inverted via the kernel, $K_2(x_2,y_2,z_2,y|u,\beta)$, which depends explicitly on χ:

$$K_2\ (x_2,y_2,z_2,y|u,\beta) = \sqrt{\frac{\beta}{2\pi}} \times \exp[-\beta u^2 x_2 + \beta u y_2 - \beta z_2 - \beta\chi(uy)]u^3.$$

Note that the multidimensionality of the kernel, K_2, is not a problem from the point of view of a χ^2 non-parametric minimisation described in Section 3.

APPENDIX B: EXTERNAL SPHERICAL ISOTROPIC CLUSTERS

Consider a satellite of our Galaxy assumed to be well described as a spherical isotropic cluster with an LF indexed by this kinematic temperature. Let $4\pi^2 A_\lambda(\mu_b, L, R)\mu\, d\mu\, \mathrm{d}L R\, \mathrm{d}R$ be the number of stars which have proper motions, $\mu^2 = \mu_b^2 + \mu_\ell^2$, and apparent luminosity L at radius R from the centre at the wavelength λ. This quantity is a convolution of the distribution function $f(\varepsilon, \beta)$ (a function of energy, ε, and $\beta \equiv 1/\sigma^2$) and the luminosity function, $g_\lambda(L_0, \beta)$, a function of the intrinsic luminosity, L_0, the population, β, and wavelength λ:

$$A_\lambda(\mu, L, R) = \int\int\int f(\varepsilon, \beta) g_\lambda(\beta, Lr'^2)\, \mathrm{d}\beta\, \mathrm{d}z\, \mathrm{d}v_z, \tag{B1}$$

which can be rearranged as

$$A_\lambda(\mu, L, R) = 4 \int\int\int f(\varepsilon, \beta) g_\lambda(\beta, Lr'^2) \times \frac{r\, \mathrm{d}r}{\sqrt{r^2 - R^2}} \frac{\mathrm{d}\varepsilon}{\sqrt{2(\psi + \varepsilon) - v^2}} \mathrm{d}\beta, \tag{B2}$$

where $v^2 = \mu^2 r'^2$ is the velocity in the plane of the sky, $r'^2 = (r^2 - R^2 + r_\odot^2)$ the distance to the observer, $r_\odot$ the distance to the cluster, and r the distance to the cluster centre. The potential can be derived non-parametrically from the projected density (using Jeans's equation). Indeed, the mass enclosed within a sphere of radius r reads

$$M_{\rm dyn}(< r) = r^2 \frac{\mathrm{d}\psi}{\mathrm{d}r} = -\frac{r^2}{\rho} \frac{\mathrm{d}(\rho\sigma^2)}{\mathrm{d}r}, \tag{B3}$$

where $\psi(r)$ is the gravitational potential, $\rho(r)$ the density, and $\sigma(r)$ the radial velocity dispersion. The surface density is related to the density via an Abel transform:

$$\Sigma(R) = \int_{-\infty}^{\infty} \rho(r)\, \mathrm{d}z = 2 \int_R^\infty \rho(r) \frac{r\, \mathrm{d}r}{\sqrt{r^2 - R^2}} \equiv \mathcal{A}_R(\rho), \tag{B4}$$

where $\Sigma(R)$ is the projected surface density, and R the projected radius as measured on the sky. Similarly, the projected velocity dispersion σ_p^2 is related to the intrinsic velocity dispersion, $\sigma^2(r)$, via the *same* Abel transform (or projection)

$$\Sigma(R)\sigma_p^2(R) = 2 \int_R^\infty \rho(r)\sigma^2(r) \frac{r\, \mathrm{d}r}{\sqrt{r^2 - R^2}} \equiv \mathcal{A}_R(\rho\sigma^2). \tag{B5}$$

Note that $\Sigma(R)\sigma_p^2$ is the projected kinetic energy density divided by 3 (corresponding to one degree of freedom), and $\rho(r)\sigma^2$ the kinetic energy density divided by 3. Inserting equations (B4) and (B5) in equation (B3) yields

$$M_{\rm dyn}(< r) = -\frac{r^2}{\mathcal{A}_r^{-1}(\Sigma)} \frac{\mathrm{d}\mathcal{A}_r^{-1}(\Sigma\sigma_p^2)}{\mathrm{d}r},$$

$$\text{while} \quad \rho(r) = \frac{1}{4\pi r^2} \frac{\mathrm{d}}{\mathrm{d}r} M_{\rm dyn}(< r) \quad \text{and} \quad \nabla^2\psi = -4\pi G\rho. \tag{B6}$$

The underlying isotropic distribution is given by an inverse Abel from the density:

$$f(\varepsilon) = \frac{1}{\sqrt{8}\pi^2} \int \frac{\mathrm{d}^2\rho}{\mathrm{d}\psi^2} \frac{\mathrm{d}\psi}{\sqrt{\varepsilon - \psi}} \equiv \int_0^\infty F(\beta) \exp(-\beta\varepsilon)\, \mathrm{d}\beta, \tag{B7}$$

where an isothermal decomposition over temperature β was assumed for the distribution function (this assumption is not required: any parametrized decomposition is acceptable). So

$$F(\beta) = \mathcal{L}^{-1}[f(\varepsilon)] = \mathcal{L}^{-1}\{\mathcal{A}^{-1}[\mathcal{A}^{-1}(\Sigma)]\}, \tag{B8}$$

where $\mathcal{L}$ is the Laplace operator.

Calling

$$G[Y] = \int_0^Y \frac{\exp(-X)\, \mathrm{d}x}{\sqrt{Y - X}} = \sqrt{\pi}\, \mathrm{Erfi}(\sqrt{Y})\, \mathrm{e}^{-Y},$$

$$g_1(\beta, Lr'^2) = g_\lambda(\beta, Lr'^2) F(\beta) \beta^{-3/2}, \tag{B9}$$

equation (B2) becomes

$$A_\lambda(\mu, L, R) = 2\sqrt{2} \int_0^\infty \left[\int_R^\infty G\left\{ \beta \left[\frac{\mu^2(r^2 - R^2 + r_\odot^2)}{2} - \psi(r) \right] \right\} \times g_1[\beta, L(r^2 - R^2 + r_\odot^2)] \frac{r\, \mathrm{d}r}{\sqrt{r^2 - R^2}} \right] \mathrm{d}\beta \tag{B10}$$

where G is a known kernel, while g_λ is the unknown LF sought. Equation (B10) is the direct analogue of equation (8). It will be invertible following the same route with *GAIA* photometry. (With today's accuracy in photometry, for a typical globular cluster at a distance $r_\odot$ of, say, 10 kpc, the relative positions within the cluster are negligible with respect to $r_\odot$: $r^2 - R^2 \ll r_\odot^2$; therefore

$$A_\lambda(\mu, L, R) = 2\sqrt{2} \int_0^\infty \left[\int_R^\infty G\left\{ \beta \left[\frac{\mu^2 r_\odot^2}{2} - \psi(r) \right] \right\} \frac{r\mathrm{d}r}{\sqrt{r^2 - R^2}} \right] \times g_1(\beta, Lr_\odot^2) \mathrm{d}\beta.$$

L is then also mute, and the inversion problem shrinks to one involving finding the relative weights, $g_L[\beta]$ of a known distribution.

This paper has been typeset from a TEX/LATEX file prepared by the author.